

A strain-wavelength modelling of low-frequency cantilever fibre Bragg grating accelerometer

Proc IMechE Part C:
J Mechanical Engineering Science
0(0) 1–13
© IMechE 2021
Article reuse guidelines:
sagepub.com/journals-permissions
DOI: 10.1177/09544062211008929
journals.sagepub.com/home/pic
SAGE

Nor Syukriah Khalid^{1,2}, Mohd Firdaus Hassan¹ ,
Mohd Hafizi Zohari¹ and Muhammad Rais Rahim¹

Abstract

The accuracy of single-degree-of-freedom (SDOF) model in describing the beam motion of low-frequency cantilever fibre Bragg grating (FBG) accelerometer can be further explored, since the SDOF model is limited to fundamental vibration modes. Therefore, this paper addresses the aforementioned limitation by introducing a modal model of the cantilever Euler-Bernoulli (EB) beam into the wavelength shift equation. This modal model (FBG-MM) considered five vibration modes. The convergent series of eigenfunction for cantilevered EB beam was solved using a standard modal expansion theory. The curvature of the cantilevered beam resulted from dual differentiation of the eigenfunction (with respect to x) is then related to the strain and wavelength of the FBG. The computed wavelength shift using FBG-MM was compared with the SDOF model. The experimental results where the harmonic base excitation occurring at five different frequencies were also discussed. The simulation results showed that the wavelength shift exhibited more reasonable behaviour along the beam particularly when the excitation frequency exceeded the second bending mode (596.67 Hz). The FBG-MM and experimental wavelength shift showed convincing correlation only when the excitation frequency came close to the fundamental frequency. On the other hand, there was no agreement at low excitation frequencies due to stiffness issues of the cantilever beam and the capability of the optical spectrum analyser. In future, the improvement of this study will focus on introducing a tip mass on the cantilever beam for increasing the accelerometer sensitivity and representing the cantilever beam using Timoshenko model.

Keywords

Fibre Bragg grating accelerometer, strain, modal model, cantilever Euler-Bernoulli beam model

Date received: 17 March 2021; accepted: 20 March 2021

Introduction

Recently, researchers have shown an increased interest in the development of fibre Bragg grating (FBG) accelerometer due to its capability to operate in harsh environmental conditions, invulnerability to electromagnetic fields, and ability to provide multiple sensing points in a single cable.¹ These criteria have enabled the FBG accelerometer to serve in many vibration monitoring systems such as in steel footbridge, military wheeled truck, gas exploration, and ground motion.^{2–5} Some of the earliest FBG accelerometer studies were presented by Tveten et al.⁶ where they had developed a simple harmonic oscillator with the sensitivity detection of less than $1 \mu\text{g}$, while Kersey et al.⁷ introduced a fibre Fabry-Perot accelerometer with high sensitivity and good linearity. The principle of Fabry-Perot in Kersey et al.⁷ was then adapted by Gerges et al.⁸ to integrate with diaphragm-type FBG accelerometer and successfully improved its

sensitivity. The diaphragm FBG accelerometer was also studied by Weng et al.⁹ with the combination of U-shaped rigid cantilever beam to enhance the vibration effect. Muller et al.¹⁰ introduced two diaphragms in FBG accelerometer design to minimise the cross-coupling of non-directional accelerations. However, their design only managed to obtain sensitivity of about 1 pm/G compared with 23.8 to 45.9 pm/G , which was obtained by Liu et al.¹¹ using two diaphragms as well but with different design. Li et al.¹² presented the latest study on diaphragm

¹Universiti Malaysia Pahang, Kuantan, Malaysia

²DRB-HICOM University of Automotive Malaysia, Pekan, Malaysia

Corresponding author:

Mohd Firdaus Hassan, Department of Mechanical Engineering, College of Engineering, Universiti Malaysia Pahang, Kuantan, Pahang, Malaysia.
Email: firdaus@ump.edu.my

FBG accelerometer with the combination of temperature compensation. Another design of FBG accelerometer was also presented by Li et al.¹³ based on a transversely rotating stick while Jiang and Yang¹⁴ successfully developed 3-axis FBG accelerometer.

From the comprehensive literature study, it was found that the most common design of FBG accelerometer is based on cantilever beam mechanism.^{2–3,15–20} However, it could easily induce strain, as FBG is more sensitive to strain and temperature due to refractive index change and grating period variation.²¹ Cantilever FBG beam mechanism basically consists of a single FBG sensor bonded on a thin cantilever beam, with or without tip mass. In this light, the presence of the tip mass improves the sensitivity of the accelerometer.¹ Furthermore, to serve as an accelerometer, this system is framed into a cubical space functioning as a housing, as shown in the close-up of cantilever FBG accelerometer in Figure 1 (b). Due to motion transfer from the housing to the beam at any point (x, t) along the beam, the dynamic strain of the beam is transferred to the FBG. The amount of FBG strain generated from the dynamic motion of the beam will produce an amount of wavelength shift that is directly proportional to the acceleration. As a complete measurement configuration, Figure 1(a) shows an experimental setup consists of shaker (base exciter), FBG accelerometer (red dots), plate (structure where acceleration is to be measured), and FBG interrogation system.

With regard to the cantilever FBG accelerometer, Peter et al.²² described that the strain of FBG can be computed by using pure bending theory²³ and

presented a static relationship between variations of applied load, F , and strain, $\varepsilon(x)$. This approach is then adapted by other researchers^{1,2,16,18,19,24} for dynamic study, in which the static force (F) is replaced by base excitation ($m \times a$), known as single-degree-of-freedom (SDOF) model. This model is based on the assumption that the base excitation is harmonic in time. However, the base excitation of cantilever beam is subject to arbitrary small rotation and translation, as shown in Figure 1(b). Moreover, by equating shear force to zero for pure bending model, the beam response for SDOF showed a linear pattern along the beam, which proved to be inaccurate compared with the advanced model, such as Timoshenko theory. In addition, the strain generated on the beam surface is proportional to the curvature of the beam and not directly related to the base acceleration. Unquestionably, once the strain has been generated and converted to wavelength shift ($\Delta\lambda$), the sensitivity of the FBG accelerometer (denoted as S) can be determined from the relationship of wavelength shift and base acceleration.

Acknowledging the aforementioned drawbacks of SDOF, the aim of this study is to introduce a more realistic mathematical model of the cantilever FBG accelerometer based on the EB beam theory, which can consider multiple modes of vibration (next section), as it has been successfully applied for piezoelectric accelerometer²⁵ and piezoelectric energy harvester.²⁶ Furthermore, there were two rationales for selecting EB model to represent cantilever FBG accelerometer: (i) low excitation frequency was used in this study; and (ii) the length to thickness ratio of the beam (l/d) was more than 20 (l/d was 125 for cantilever beam used in this study). If these two criteria are not fulfilled, the EB model would be invalid and Timoshenko (T) beam model should be used instead. The T model considers shear force and rotational inertia of the beam, making it suitable for describing small l/d ratio (short and thick beam) for all excitation frequencies (regardless of low or high frequencies). The dynamic response of these two models (EB and T) have been discussed in a preliminary study by previous authors.²⁷ The representation of T model into cantilever FBG accelerometer will be considered in future study and presented in the next publication.

In addition, an accurate strain equation of the cantilever FBG accelerometer will be derived from the standard strain theory under dynamic motion obtained from EB model, thus resulting in accurate sensitivity of the accelerometer, as discussed in the Strain-curvature relationship and sensitivity of cantilever FBG accelerometer section. Unlike the works in references^{1,2,16,18,19,24} which considered tip mass beam for increasing the accelerometer's sensitivity, this study can only be compared with the work done by Lam et al.³⁰ for non-tip mass beam. Apart from introducing tip mass onto the cantilever, some

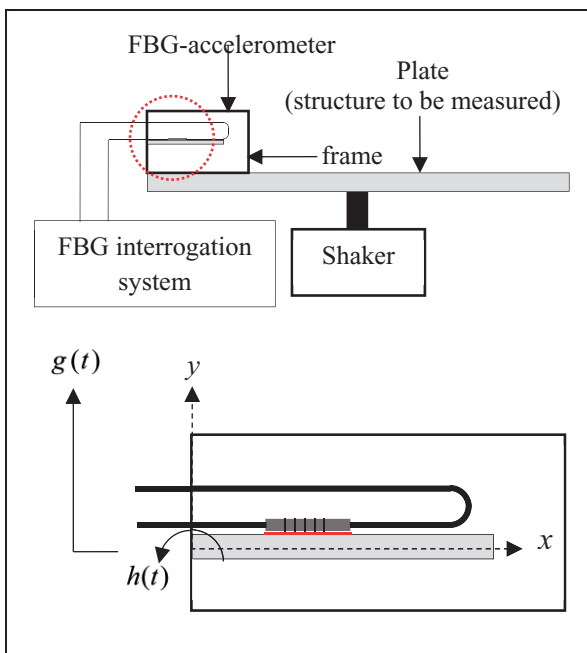


Figure 1. (a) Measurement configuration using cantilevered beam FBG accelerometer; and (b) Close-up of cantilevered FBG accelerometer (red dotted circle) under translational and rotational base motions.

researchers^{15,16} suggested the use of patch thickness to alter the distance between axis of the FBG sensor to the neutral axis of the cantilever for increasing the accelerometer's sensitivity.

The scope of this study is limited to wavelength shift comparison between simulation and experiment, objectively to demonstrate the feasibility of the FBG-MM on the cantilever FBG accelerometer. The acceleration measurement produced from the experimental work and its comparison with commercial accelerometer, e.g., piezoelectric type, as well as the sensitivity studies that will be discussed in the next publication.

The next section describes the theoretical model of the cantilever EB beam. And then the strain-curvature relationship and sensitivity model of the cantilever FBG accelerometer are presented. The Experimental description section presents the cantilever FBG accelerometer and the test rig. The Results and discussion of FBG-MM and SDOF model section and the Validation of FBG-MM against experimental data section present and discuss the theoretical and experimental results, respectively.

Steady-state response of cantilevered Euler-Bernoulli beam model under harmonic base excitation using modal model approach

As shown in Figure 1(b), the equation of motion of EB beam for undamped free vibration can be written as below:²⁹

$$EI \frac{\partial^4 u(x, t)}{\partial x^4} + m \frac{\partial^2 u(x, t)}{\partial t^2} = 0 \quad (1)$$

where, E , I , and m are the Young's modulus, mass moment of inertia, and mass per unit length, respectively. Appendix 1 can be referred to for detailed derivation of equation (1). The absolute motion of the beam can be represented by:

$$u_{abs}(x, t) = u_b(x, t) + u_{rel}(x, t) \quad (2)$$

where, $u_{rel}(x, t)$ is the transverse displacement relative to the clamped end of the beam; while the base motion $u_b(x, t)$ is a combination of transverse base displacement $g(t)$ and small base rotation of the beam $h(t)$, as given by equation (3) and illustrated in Figure 2.

$$u_b(x, t) = \delta_1(x)g(t) + \delta_2(x)h(t) \quad (3)$$

For cantilever beam, $\delta_1(x) = 1$ and $\delta_2(x) = x$ represent the displacement influence functions. Under viscous air (medium) and Kelvin-Voigt (or strain-rate) damping and considering the relative motion $u_{rel}(x, t)$, the damped equation of motion for the

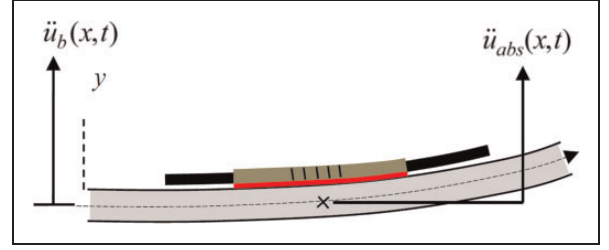


Figure 2. Absolute motion of FBG due to base motion accelerated by shaker.

cantilever EB beam model subject to arbitrary base motion is given as:

$$\begin{aligned} EI \frac{\partial^4 u_{rel}(x, t)}{\partial x^4} + c_s I \frac{\partial^5 u_{rel}(x, t)}{\partial x^4 \partial t} + c_a \frac{\partial u_{rel}(x, t)}{\partial t} \\ + m \frac{\partial^2 u_{rel}(x, t)}{\partial t^2} \\ = -m \frac{\partial^2 u_b(x, t)}{\partial t^2} - c_a \frac{\partial u_b(x, t)}{\partial t} \end{aligned} \quad (4)$$

where, c_a and c_s are viscous air and strain-rate damping coefficient per unit length. Appendix 1 can be made a reference for detailed derivation from equations (1) to (4). The boundary conditions for relative vibratory motion of the beam are:

$$u_{rel}(0, t) = 0, \quad \frac{\partial u_{rel}(x, t)}{\partial x} \Big|_{x=0} = 0 \quad (5a, b)$$

$$\left[EI \frac{\partial^2 u_{rel}(x, t)}{\partial x^2} + c_s I \frac{\partial^3 u_{rel}(x, t)}{\partial x^2 \partial t} \right]_{x=L} = 0 \quad (5c)$$

$$\left[EI \frac{\partial^3 u_{rel}(x, t)}{\partial x^3} + c_s I \frac{\partial^4 u_{rel}(x, t)}{\partial x^3 \partial t} \right]_{x=L} = 0 \quad (5d)$$

The solution of equation (4) can be expressed by a convergent series of eigenfunction (equation (6)) solved through modal expansion method, as used by the corresponding author in solving foil structure motion in foil-air bearing problem:³⁰

$$u_{rel}(x, t) = \sum_{r=1}^{\infty} \varphi_r(x) \eta_r(t) \quad (6)$$

where, $\varphi_r(x)$ and $\eta_r(t)$ are the mass normalised eigenfunction and the modal coordinate of the clamped-free beam for the r -th mode, respectively. Since the system is proportionally damped, the eigenfunction denoted by $\varphi_r(x)$ is indeed the mass normalised eigenfunction of the corresponding undamped free vibration problem with the clamped-free boundary conditions.

$$u_{rel}(0, t) = 0, \quad \frac{\partial u_{rel}(x, t)}{\partial x} \Big|_{x=0} = 0 \quad (7a, b)$$

$$EI \frac{\partial^2 u_{rel}(x, t)}{\partial x^2} \Big|_{x=L} = 0, \quad EI \frac{\partial^3 u_{rel}(x, t)}{\partial x^3} \Big|_{x=L} = 0 \quad (7c,d)$$

Therefore, the resulting mass normalised eigenfunction of the r -th mode is:

$$\varphi_r(x) = \sqrt{\frac{1}{mL}} \left[\cosh \frac{\lambda_r}{L} x - \cos \frac{\lambda_r}{L} x - \sigma_r \left(\sinh \frac{\lambda_r}{L} x - \sin \frac{\lambda_r}{L} x \right) \right] \quad (8)$$

where, λ_r is the dimensionless frequency numbers obtained from the characteristic equation given by:

$$\sigma_r = \frac{\sinh \lambda_r - \sin \lambda_r}{\cosh \lambda_r + \cos \lambda_r} \quad (9)$$

The mass normalised eigenfunction given by equation (8) satisfies the orthogonality conditions:

$$\int_{x=0}^L m \varphi_s(x) \varphi_r(x) dx = \delta_{rs}, \quad (10, 11)$$

$$\int_{x=0}^L EI \varphi_s(x) \frac{d^4 \varphi_r(x)}{dx^4} dx = \omega_r^2 \delta_{rs}$$

where, δ_{rs} is the Kronecker delta and is defined as being equal to unity for $s = r$ and equal to zero for $s \neq r$, and ω_r is the undamped natural frequency of the r -th mode given by:

$$\omega_r = \lambda_r^2 \sqrt{\frac{EI}{mL^4}} \quad (12)$$

The two terms in the right-hand-side (RHS) of the equation (4) are left as external excitations. The modal response of the equation (4) is obtained by adapting the orthogonality conditions as given by equations (10) and (11) (see Appendix 2 for detailed conversion of equations (4) to (13)), thus yielding:

$$\frac{\partial^2 \eta_r(t)}{\partial t^2} + \left(\frac{c_s \omega_r^2}{E} + \frac{c_a}{m} \right) \frac{\partial \eta_r(t)}{\partial t} + \omega_r^2 \eta_r(t) = -m \frac{\partial^2 u_b(x, t)}{\partial t^2} - c_a \frac{\partial u_b(x, t)}{\partial t} \quad (13)$$

For undamped system, the equation (13) reduces to ($c_a = 0$ and $c_s = 0$):

$$\frac{\partial^2 \eta_r(t)}{\partial t^2} + \omega_r^2 \eta_r(t) = -m \frac{\partial^2 u_b(x, t)}{\partial t^2} \quad (14)$$

Let the base excitation consists of transverse displacement and small rotation about clamped end, thus:

$$-m \frac{\partial^2 u_b(x, t)}{\partial t^2} = -m \left(\gamma_r^w \frac{\partial^2 g(t)}{\partial t^2} + \gamma_r^\theta \frac{\partial^2 h(t)}{\partial t^2} \right) \quad (15)$$

where,

$$\gamma_r^w = \int_{x=0}^L \varphi_r(x) dx, \quad \gamma_r^\theta = \int_{x=0}^L x \varphi_r(x) dx \quad (16)$$

Considering only inertial excitation without rotational base excitation ($h(t) = 0$), the modal response is written as:

$$\frac{\partial^2 \eta_r(t)}{\partial t^2} + \omega_r^2 \eta_r(t) = -m \gamma_r^w \frac{\partial^2 g(t)}{\partial t^2} \quad (17)$$

Let $g(t) = U_0 e^{i\omega t}$ and $\eta_r(t)$ is expected to be harmonic ($\eta_r(t) = \eta_r e^{i\omega t}$), hence:

$$-\omega^2 \eta_r e^{i\omega t} + \omega_r^2 \eta_r e^{i\omega t} = m \gamma_r^w \omega^2 U_0 e^{i\omega t} \quad (18)$$

where,

$$\frac{\partial^2 (U_0 e^{i\omega t})}{\partial t^2} = -\omega^2 U_0 e^{i\omega t} \quad \text{and} \quad \frac{\partial^2 (\eta_r e^{i\omega t})}{\partial t^2} = -\omega^2 \eta_r e^{i\omega t}$$

From equation (18), the steady-state solution of equation (14) becomes:

$$\eta_r(t) = \frac{m \gamma_r^w \omega^2 U_0}{\omega_r^2 - \omega^2} e^{i\omega t} \quad (19)$$

It is known that:

$$\gamma_r^w = \int_{x=0}^L \varphi_r(x) dx = \frac{2\sigma_r}{\lambda_r} \sqrt{\frac{L}{m}} \quad (20)$$

where, equation (19) becomes:

$$\eta_r(t) = \frac{m \omega^2 U_0}{\omega_r^2 - \omega^2} \frac{2\sigma_r}{\lambda_r} \sqrt{\frac{L}{m}} e^{i\omega t} \quad (21)$$

Substituting equations (8) and (21) into equation (6), it yields:

$$u_{rel}(x, t) = \sum_{r=1}^{\infty} \sqrt{\frac{1}{mL}} \left[\cosh \frac{\lambda_r}{L} x - \cos \frac{\lambda_r}{L} x - \sigma_r \left(\sinh \frac{\lambda_r}{L} x - \sin \frac{\lambda_r}{L} x \right) \right] \times \frac{m \omega^2 U_0 2\sigma_r}{\omega_r^2 - \omega^2} \sqrt{\frac{L}{m}} e^{i\omega t} \quad (22)$$

After re-arranging equation (22), the relative motion of cantilever EB beam finally yields:

$$u_{rel}(x, t) = 2U_0 e^{i\omega t} \sum_{r=1}^{\infty} \left(\left[\cosh \frac{\lambda_r}{L} x - \cos \frac{\lambda_r}{L} x - \sigma_r \left(\sinh \frac{\lambda_r}{L} x - \sin \frac{\lambda_r}{L} x \right) \right] \right)$$

$$\times \frac{\sigma_r \omega^2}{\lambda_r \omega_r^2 - \omega^2} \quad (23)$$

Equation (23) is used for determining the curvature of the beam, which is required to compute the strain and wavelength shift of the FBG accelerometer, as explained in the next section.

Strain-curvature relationship and sensitivity of cantilever FBG accelerometer

Based on the bending strain equation under dynamic motion³¹ and referring to work in Erturk et al.,³² the strain generated by the FBG is given as:

$$\varepsilon_{FBG}(x, t) = -(h + h_f) \frac{\partial^2 u_{rel}(x, t)}{\partial x^2} \quad (24)$$

where, h and h_f are half-thickness of beam and FBG, respectively; and $\frac{\partial^2 u_{rel}(x, t)}{\partial x^2}$ is the curvature of the beam resulting from dual differentiation of equation (23), completely written as:

$$\begin{aligned} \frac{\partial^2 U_{rel}(x, t)}{dx^2} = & 2U_0 e^{i\omega t} \sum_{r=1}^{\infty} \left(\frac{\lambda_r}{L} \right)^2 \left(\left[\cosh \frac{\lambda_r}{L} x + \cos \frac{\lambda_r}{L} x \right. \right. \\ & \left. \left. - \sigma_r \left(\sinh \frac{\lambda_r}{L} x + \sin \frac{\lambda_r}{L} x \right) \right] \right) \\ & \times \frac{\sigma_r \omega^2}{\lambda_r \omega_r^2 - \omega^2} \end{aligned} \quad (25)$$

It is important to assume that the FBG is perfectly bonded to the beam's surface. Assuming that adhesive between the FBG and the beam is to be considered, the half-thickness of adhesive should be included in equation (24). As observed from equation (24), the strain also depends on the location where the FBG is attached to; more analysis is needed in this aspect. It is known that the wavelength shift of the FBG is directly proportional to the strain of the FBG as given in equation (26):^{15,16}

$$\Delta\lambda \approx 1.2 \times \varepsilon_{FBG} \quad (26)$$

where, 1.2 is strain sensitivity for FBGs with peak wavelengths in the C band regime (1.2 pm/ $\mu\epsilon$ in general). From both derivations in the previous section and this section, the sensitivity of the FBG accelerometer can be written as:

$$S = \frac{\Delta\lambda}{\ddot{u}_b(x, t)} = \frac{1.2 \times \varepsilon_{FBG}}{\ddot{u}_b(x, t)} \quad (27)$$

In the work done by Lam et al.,²⁸ the FBG strain, ε_{FBG} (see equation (28)) is linear along the beam and cannot be assumed to be uniform, as it is a function of position of FBG sensor (x) and time (t). In addition, the sensitivity of the FBG accelerometer is also linear, since it depends on the position of the FBG sensor (x) as well but is no longer dependent on time (t); this is attributable substituting equation (28) into equation (27), which produces equation (29).

$$\varepsilon_{FBG} = \frac{6(L-x)m}{bd^2E} \ddot{u}_b(x, t) \quad (28)$$

$$S = \frac{7.2(L-x)m}{bd^2E} \quad (29)$$

In this paper, substituting equation (24) into equation (27) yields a non-linear sensitivity (or uniform), but rather, to be relied on the forcing frequency of the system, ω . Therefore, it is noted that the research on the sensitivity of FBG accelerometer can be furthered explored, thereby leading to better understanding of the FBG behaviour.

Experimental description

Figure 3 and Table 1 show the dimensions and properties of cantilever beam. For experimental purpose, the dimensions of the beam were almost similar to the work in references,^{15,16} except the length of the beam was increased to 50 mm because of two reasons: (i) to produce as small as possible the fundamental frequency (longer beam produces smaller fundamental

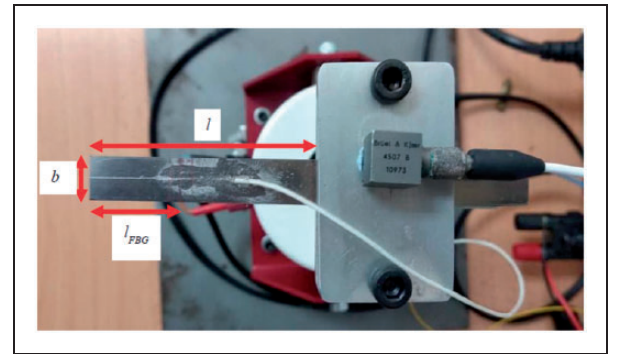


Figure 3. Dimensions of cantilever beam.

Table 1. Properties of cantilever beam.

Length, l	50 mm
Width, b	10 mm
Thickness, d	0.3 mm
Location of centre of FBG measured from free end, l_{FBG}	20 mm
Density, ρ	8000 kg/m ³
Young's modulus, E	193 GPa
Poisson ratio, ν	0.29

frequencies); and (ii) to ease the attachment of the FBG sensor onto the beam. The FBG sensor was attached 20 mm from the free end of the cantilever beam. Figure 4 and Table 2 show the experimental setup and item description for the cantilever FBG accelerometer measurement. A simple sinusoidal harmonic excitation at the frequency of 20, 40, 60, 80, and 90 Hz at the same magnitude of acceleration ($\approx 4 \text{ m/s}^2$) was generated by a portable electrodynamic shaker (1). The excitation input was channelled from DASYLAB software through output module NI9236 (8). The cantilever FBG accelerometer (2) was mounted on a simple clamping mechanism and connected to the portable electrodynamic shaker by a rigid stinger. The excitation output was measured by a single axial piezoelectric accelerometer (8) to ensure the output given by the shaker was as desired. The recorded acceleration will be dual-integrated to produce its displacement before it was fed into equation (23) as the base excitation input to the simulation FBG-MM. Then, it was fed into the SDOF model proposed by Lam et al.²⁸ for comparative study. The FBG sensor was connected to a circulator (4) as a junction to FBG interrogator (5) and a light source (6). The wavelength shift signal was channelled to computer and processed in FBG analyser SENSE2020 V1.6.3.3. Since the FBG is also sensitive to changes in temperature, the experimental work was carried out in controlled room, where the temperature was approximately 22 °C.

Encapsulation of FBG onto the beam

The recent works done by Liu et al.³³ has proved that the double-point encapsulation has increased the sensitivity of the FBG accelerometer and prevented FBG

spectrum chirp and wavelength split, compared with the embedded encapsulation method, where the FBG is fully attached the beam, as presented in this paper. However, this work chose the embedded encapsulation because of the following reasons:

- (i) From the authors' experience, since the response (deflection) of cantilever beam at low frequency is very small, the induced strain is also very small and it does not create FBG spectrum chirp and wavelength split;
- (ii) The FBG grating was completely attached onto the beam; and
- (iii) For the cantilever beam mechanism, there is a possibility of buckling occurring on the FBG if double-point encapsulation is used (double-point encapsulation lets the grating area move freely).

Table 2. Item description of the experimental setup in Figure 4.

Item No.	Description
1	Portable electrodynamic shaker GW-V4/PA30E
2	Fibre Bragg grating sensor 1544 nm (grating length is 5 mm)
3	Single axial accelerometer <i>Brüel & Kjær Type 4507B</i>
4	Circulator
5	Optical spectrum analyser FBGA-F-1510-1590-FA
6	Light source
7	NI 9234 C series sound and vibration input module
8	NI9269 C series voltage output module

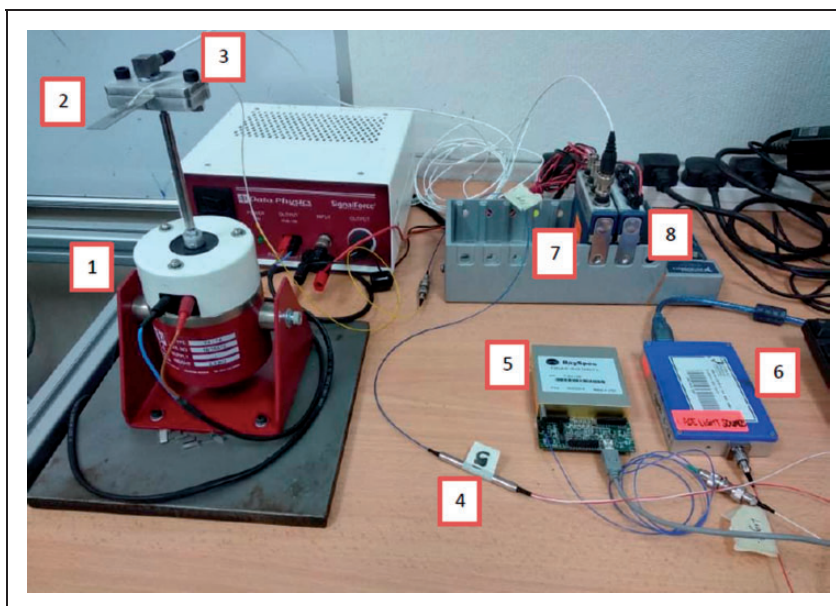


Figure 4. Experimental setup.

Results and discussion of FBG-MM and SDOF model

Figure 5 shows the strain and wavelength shift of the FBG along the beam at a specific time ($t = 1.0138$ s) with different excitation frequencies (20, 40, 60, 80, and 90 Hz) computed using SDOF model²⁸ and FBG-MM with number of modes considered as five. For both models, the maximum and minimum strains occurred at the clamped and free ends, respectively, as shown in the left column of Figure 5. With regard to basic pure bending, this phenomenon fulfilled the criterion of zero-moment when x approached the maximum length of the beam ($\lim_{x \rightarrow L} M = 0$) while maximum-moment was generated when x was zero. Considering multiple mode of vibrations, FBG-MM depicted more reasonable strain pattern from the clamped to free ends while SDOF model showed linear strain (imagine if the cantilever beam is bent, it will show curved-deflection). Moreover, this strain pattern can be observed clearly if the FBG

accelerometer was excited beyond the first bending mode, e.g., 600 Hz (close to the second bending mode), as shown in Figure 8, which will be discussed with respect to aforementioned figure. The wavelength shift showed similar pattern (right column of Figure 5) to the strain, since they are proportionally linear, as written in equation (26). On the other hand, the strain and the wavelength shift increased in accordance with the excitation frequencies.

Figure 6(a) to (e) show the wavelength shift plots against time, where x is 20 mm measured from free end of the cantilever beam at different excitation frequencies; while Figure 7 shows the base acceleration input for the excitation frequency of 90 Hz (Figure 6 (e) is its result). Generally, by fixing the maximum peak of base displacement for all excitation frequencies, the acceleration increases as the excitation frequency increases, resulting in the increment of the wavelength shift. This can be seen at 20 Hz, when the maximum strain generated was roughly 78 pm and 17 pm for both methods, while at 90 Hz, it

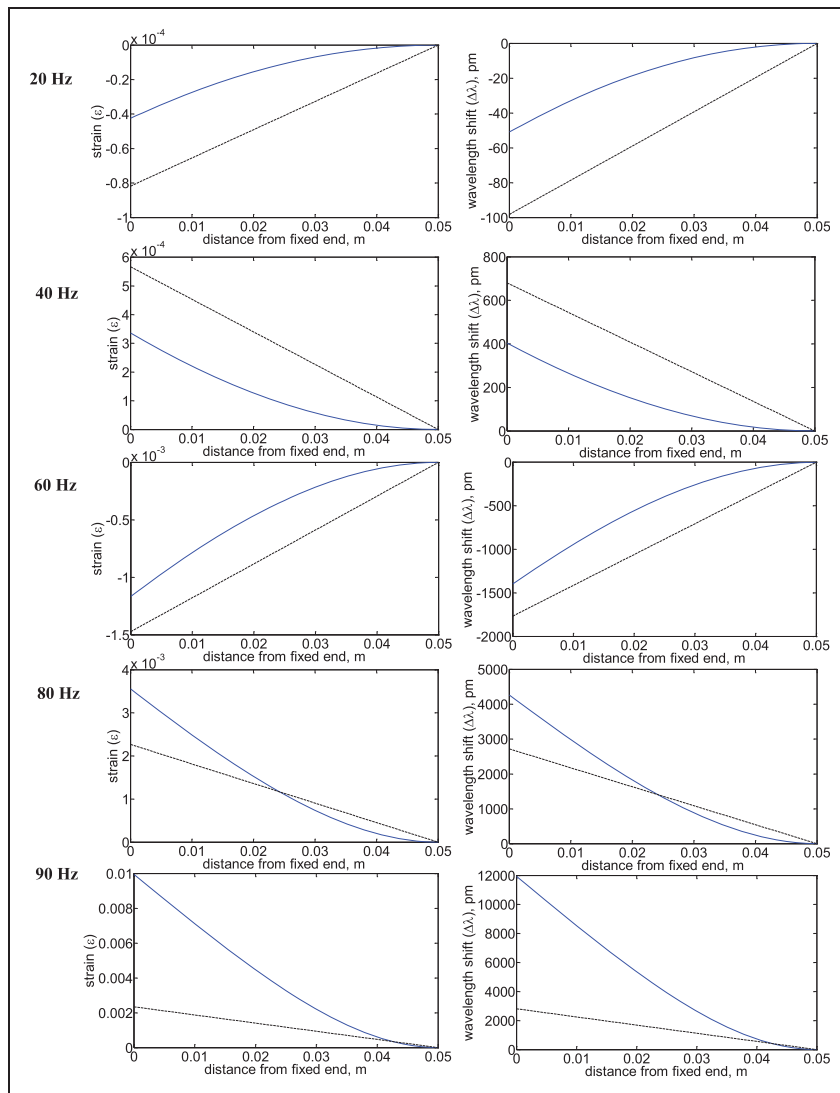


Figure 5. Strain (left column) and wavelength shift (right column) of the FBG sensor (solid line and blue plot – FBG-MM & dash and black plot – SDOF model).

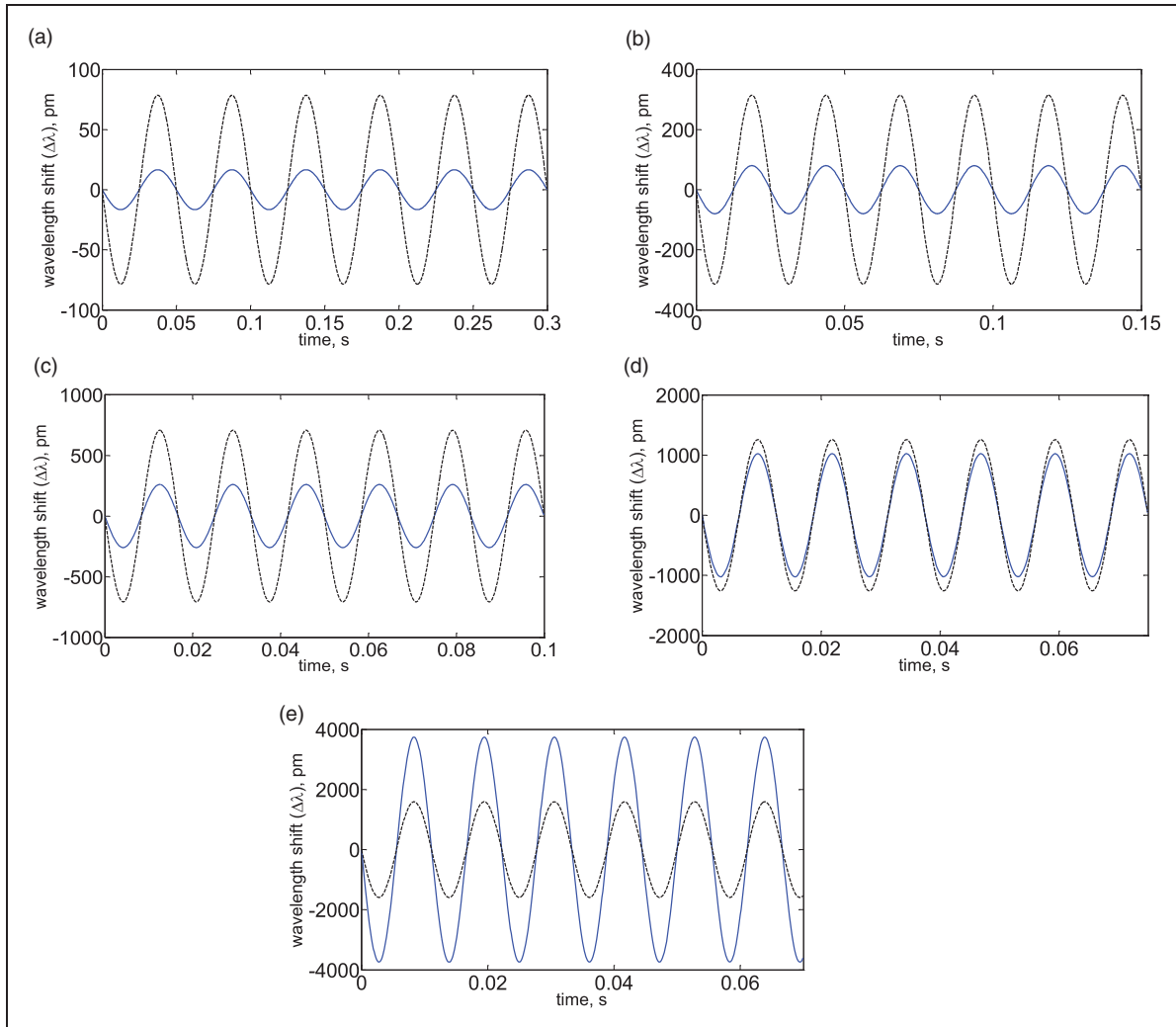


Figure 6. Wavelength shift of the FBG sensor at $x = 20$ mm from free end at a specific range of time at different excitation frequencies (solid line and blue plot – FBG-MM and dash and black plot – SDOF model).

reached 3741 pm and 1600, respectively. The SDOF model³⁰ overestimated the wavelength shift compared to FBG-MM. However, this was inconclusive because at other excitation frequencies, the strain was underestimated. This was observed in Figure 5, at the excitation of 80 and 90 Hz, especially when x was close to clamped end. However, both models showed similar patterns and were in a phase, but they both led the base acceleration by 180° phase, as shown in Figures 6(e) and 6.

In Figure 5, the strain and wavelength shift showed a decrease from clamped to free ends, as the excitation frequencies were less than the first bending mode, with some non-linear pattern depicted by the FBG-MM. The pattern, however, can be seen clearly when the excitation frequency was greater than the second bending mode e.g., 600 Hz (the second bending mode was 596.67 Hz), where the wavelength shift displayed a fluctuating pattern from clamped to free ends, as shown on the second column of Figure 8. This result can be debated, since the EB model is not appropriate for high-frequency excitation. However, the

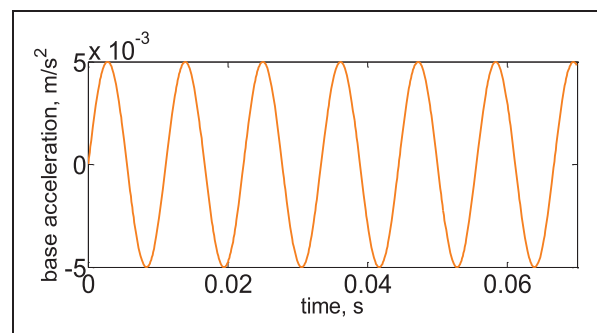


Figure 7. Base acceleration signal at 90 Hz.

employment of the best candidate of T model will yield similar fluctuating pattern to that of an EB model but with some discrepancies. Reference can be to the authors' preliminary study, which examined the strain pattern of the cantilever beam²⁷ using EB and T beam models). As expected, for SDOF model,²⁸ no matter how high the excitation frequency was, the pattern of the wavelength shift remained

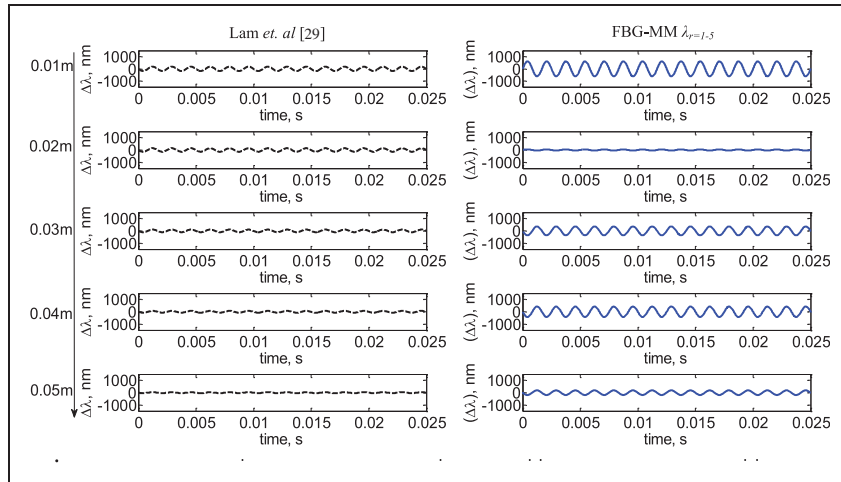


Figure 8. Wavelength shift of the FBG sensor at different positions on the beam at a specific range of time at the frequency of 600 Hz (solid line and blue plot – FBG-MM and dash and black plot – SDOF model).

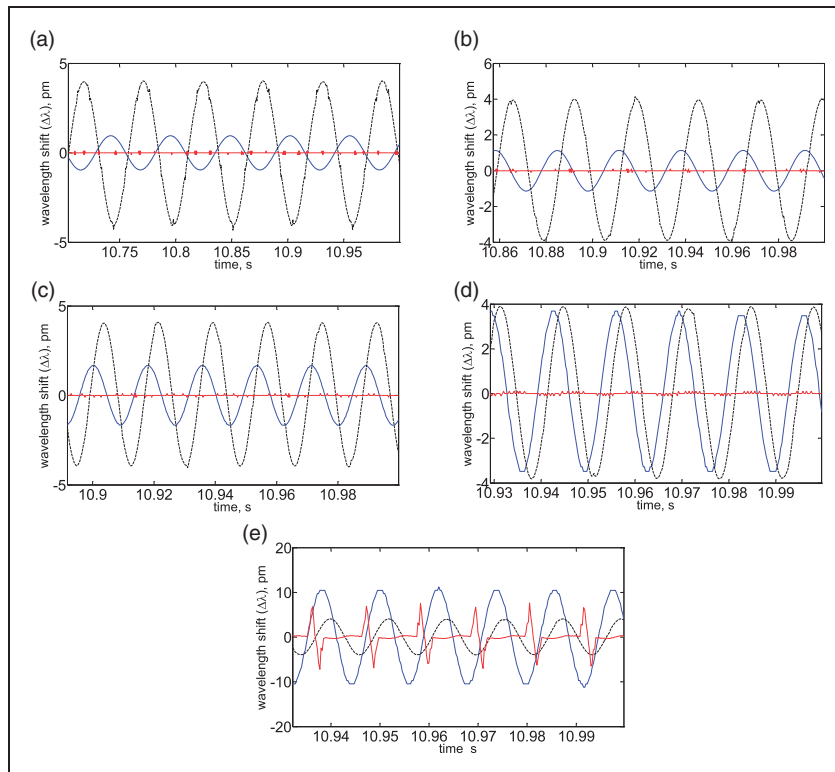


Figure 9. Wavelength shift of the FBG sensor at different excitation frequencies (solid line and blue plot – FBG-MM, dash and black plot – SDOF model and dotted and red plot – experimental data).

linear from clamped to free ends, as shown on the first column of Figure 8.

Validation of FBG-MM against experimental data

The experimental wavelength shift (red plot) and its comparison with simulation FBG-MM (blue plot) and SDOF model (black plot) of the cantilever

FBG accelerometer are shown in Figure 9. The measurement time was set to 11 seconds and for analysis purpose, the steady state results at the final second of measurement were considered. The same input data (base acceleration) used in experimental works were taken and incorporated into equation (23) as base excitation (base acceleration was first converted to base displacement) for FBG-MM and also for SDOF model. At low excitation frequencies (20, 40, 60, and 80 Hz), the experimental wavelength shift

showed poor correlation compared to FBG-MM and SDOF model. This is due to two reasons: (i) the high stiffness of beam led to small deflection when it was excited at low excitation frequencies; and (ii) since the maximum sampling rate of the optical spectrum analyser was only 5000 Hz, this resolution was inadequate to detect the wavelength shift. However, at the excitation frequency of 90 Hz, the experimental wavelength shift inclined to demonstrate similar pattern with FBG-MM, while SDOF model underestimated the wavelength shift. It should be mentioned that when excitation frequency was close to the first natural frequency of the beam (first bending mode was 95.6 Hz), the cantilever beam closely behaved as bending motion which created high curvature, thus producing convincing wavelength shift, as seen in Figure 9(e). Nonetheless, the second aforementioned reason (resolution issue) could be attributed to the notable discrepancies of the wavelength shift amplitude, shape, and phase between experimental and FBG-MM. It is also noted that the validation was not done for the excitation frequency greater than 90 Hz. By considering the working principle of common accelerometer, when the excitation frequency is around its region of natural frequency (95.6 Hz), it can cause the vibration signals to appear much higher than they actually are. When exceeding this region, the excitation frequency cantilever beam will fall under isolation region, where the signal or response of the FBG might loss. It can be observed that the duty cycle of the wavelength shift obtained from experiment is less than what is obtained from FBG-MM, where this also reflects to their output frequency. It is found that the output frequency of the wavelength shift obtained from experiment and FBG-MM is 100 Hz and 90 Hz, respectively. The most probable reason for this issue is systematics errors, which cannot be determined at the time of writing this paper. The comparison between acceleration from piezoelectric and FBG accelerometer (as presented in references^{2,34}) was not able to be demonstrated in this paper, as the focus of this study is to present an accurate model to represent the cantilever FBG accelerometer.

Conclusion

This paper demonstrated the successful implementation of EB beam model as a representation of the cantilever FBG accelerometer. In this regard, the modal model (FBG-MM) of the cantilever EB beam can consider multiple modes of vibration and adequately describe the beam motion/curvature. The strain of the FBG had been successfully correlated to the beam's relative curvature, resulting in the accurate wavelength shift of the FBG accelerometer. The FBG-MM was proven to be convincing when validated against experimental wavelength shift. However, it needs improvements in future work, e.g., resizing the

dimension of the cantilever beam to lower the natural frequencies and adding tip mass onto the cantilever beam to increase the sensitivity of the FBG accelerometer. At this stage, the acceleration and sensitivity comparison were not able to be explored, as this study only focused on the feasibility of the FBG-MM model as a replacement of the cantilever FBG accelerometer. Since the EB model was only valid for low excitation frequencies, Timoshenko model will be considered in the next publication to perfectly model the cantilever FBG accelerometer.

Declaration of Conflicting Interests

The author(s) declared no potential conflicts of interest with respect to the research, authorship, and/or publication of this article.

Funding

The author(s) disclosed receipt of the following financial support for the research, authorship, and/or publication of this article: The Ministry of Education Malaysia for their financial support through FRGS/1/2018/TK03/UMP/02/29 (RDU190191) grant scheme and MyBrain15 programme. The authors also acknowledge the Universiti Malaysia Pahang for their financial support through RDU180387 grant scheme. Data related to the research presented in this paper shall be made available through the University Malaysia Pahang's Institutional Repository.

ORCID iD

Mohd Firdaus Hassan  <https://orcid.org/0000-0002-6468-8778>

References

1. Basumallick N, Biswas P, Chakraborty R, et al. Fibre Bragg grating based accelerometer with extended bandwidth. *Meas Sci Technol* 2016; 27: 035008.
2. Gagliardi G, Salza M, Ferraro P, et al. Design and test of a laser-based optical-fiber Bragg-grating accelerometer for seismic applications. *Meas Sci Technol* 2008; 19: 085306.
3. Zhang Y, Li S, Yin Z, et al. *Fiber Bragg grating sensors for seismic wave detection, Bruges, Belgium-Deadline past*. USA: International Society for Optics and Photonics, 2005, pp.1008–1011.
4. da Costa Antunes PF, Lima HF, Alberto NJ, et al. Optical fiber accelerometer system for structural dynamic monitoring. *IEEE Sensors J* 2009; 9: 1347–1354.
5. Zhang Y, Li S, Yin Z, et al. Fiber-Bragg-grating-based seismic geophone for oil/gas prospecting. *Opt Eng* 2006; 45: 084404–084404.
6. Tveten A, Dandridge A, Davis C, et al. Fibre optic accelerometer. *Electron Lett* 1980; 16: 854–856.
7. Kersey A, Jackson D and Corke M. A simple fibre Fabry-Perot sensor. *Opt Commun* 1983; 45: 71–74.
8. Gerges A, Newson T, Jones JD, et al. High-sensitivity fiber-optic accelerometer. *Opt Lett* 1989; 14: 251–253.
9. Weng Y, Qiao X, Guo T, et al. A robust and compact fiber Bragg grating vibration sensor for seismic measurement. *IEEE Sensors J* 2012; 12: 800–804.

10. Muller MS, Buck TC and Koch AW. Fiber Bragg grating-based acceleration sensor. In: *2009 international symposium on optomechatronic technologies, 2009 ISOT*. USA: IEEE, 2009, pp.127–132.
11. Liu Q, Qiao X, Jia Z, et al. Large frequency range and high sensitivity fiber Bragg grating accelerometer based on double diaphragms. *IEEE Sensors J* 2014; 14: 1499–1504.
12. Li T, Tan Y, Han X, et al. Diaphragm based fiber Bragg grating acceleration sensor with temperature compensation. *Sensors* 2017; 17: 218.
13. Li K, Chan TH, Yau MH, et al. Fiber Bragg grating accelerometer based on a transversely rotating stick. *Optik* 2015; 126: 4337–4341.
14. Jiang Q and Yang M. Simulation and experimental study of a three-axis fiber Bragg grating accelerometer based on the pull–push mechanism. *Meas Sci Technol* 2013; 24: 115105.
15. Basumallick N, Biswas P, Dasgupta K, et al. Design optimization of fiber Bragg grating accelerometer for maximum sensitivity. *Sens Actuators A Phys* 2013; 194: 31–39.
16. Basumallick N, Chatterjee I, Biswas P, et al. Fiber Bragg grating accelerometer with enhanced sensitivity. *Sens Actuators A Phys* 2012; 173: 108–115.
17. Zhang J, Xiong Y and Yang A. Study of FBG application in acceleration sensing. In: *IEEE 9th international conference on properties and applications of dielectric materials*, 2009, pp.19–23.
18. Zhang W-g, Wu Z-g, Liu Y-g, et al. Principles and realizations of FBG wavelength tuning with elastic beams. *Optoelectr Lett* 2005; 1: 5–9.
19. Zhu Y, Shum P, Lu C, et al. Fiber Bragg grating accelerometer with temperature insensitivity. *Microw Opt Technol Lett* 2003; 37: 151–153.
20. Kalenik J and Pająk R. A cantilever optical-fiber accelerometer. *Sens Actuators A Phys* 1998; 68: 350–355.
21. Du J and He Z. Sensitivity enhanced strain and temperature measurements based on FBG and frequency chirp magnification. *Opt Express* 2013; 21: 27111–27118.
22. Fuhr PL, Spammer SJ and Zhu Y. A novel signal demodulation technique for chirped Bragg grating strain sensors. *Smart Mater Struct* 2000; 9: 85–94.
23. Huebner KH. *The finite element method for engineers*. Hoboken: John Wiley & Sons, 2001.
24. Zhu Y, Shum P, Lu C, et al. Temperature-insensitive fiber Bragg grating accelerometer. *IEEE Photon Technol Lett* 2003; 15: 1437–1439.
25. Kollias A and Avaritsiotis J. A study on the performance of bending mode piezoelectric accelerometers. *Sens Actuators A Phys* 2005; 121: 434–442.
26. Erturk A and Inman DJ. On mechanical modeling of cantilevered piezoelectric vibration energy harvesters. *J Intell Mater Syst Struct* 2008; 19: 1311–1325.
27. Khalid NS, Hassan MFB and Hafizi ZM. Dynamic characteristics and response of low frequency cantilever beam-based FBG accelerometer under base excitation. *AIP Conf Proc* 2019; 2059: 020049.
28. Lam TT, Gagliardi G, Salza M, et al. Optical fiber three-axis accelerometer based on lasers locked to π phase-shifted Bragg gratings. *Meas Sci Technol* 2010; 21: 094010.
29. Timoshenko S, Young D and Weaver W. *Vibration problems in engineering*. New York: John Wiley and Sons, Inc., 1974.
30. Bin Hassan MF and Bonello P. A new modal-based approach for modelling the bump foil structure in the simultaneous solution of foil-air bearing rotor dynamic problems. *J Sound Vib* 2017; 396: 255–273.
31. Beer FP, Russel Johnston JE and Dewolf JT. *Mechanics of materials*. New York: McGraw-Hill, 2002.
32. Erturk A, Tarazaga PA, Farmer JR, et al. Effect of strain nodes and electrode configuration on piezoelectric energy harvesting from cantilevered beams. *J Vib Acoust* 2009; 131: 011010.
33. Liu Q, He X, Qiao X, et al. Design and modelling of a high sensitivity fiber Bragg grating-based accelerometer. *IEEE Sensors J* 2019; 19: 5439–5445.
34. Ge Y, Kuang KS and Quek ST. Development of a low-cost bi-axial intensity-based optical fibre accelerometer for wind turbine blades. *Sens Actuators A Phys* 2013; 197: 126–135.

Appendix

Notation

b	width of beam
c_a	viscous air damping coefficient
c_s	strain-rate damping coefficient
d	thickness of beam
E	Young's modulus
h_f	half-thickness of FBG
h	half-thickness of beam
I	mass moment of inertia
l	length of beam
l_{FBG}	location of centre of FBG measured from free end
m	mass per unit length
r	mode number
$u_{rel}(x, t)$	the transverse displacement relative to the clamped end of the beam
$u_b(x, t)$	combination of transverse base displacement $g(t)$ and small base rotation of the beam $h(t)$
$U_0 e^{i\omega t}$	function of base excitation
V	shear force
$\delta_2(x)$ & $\delta_2(x)$	displacement influence functions
δ_{rs}	Kronecker delta
$\Delta\lambda$	wavelength shift
ε_{FBG}	strain generated by FBG
$\eta_r(t)$	modal coordinate of the clamped-free beam for the r -th mode
$\varphi_r(x)$	mass normalised eigenfunction of the clamped-free beam for the r -th mode
λ_r	dimensionless frequency numbers
ν	Poisson's ratio

ρ	density
σ_r	a constant for mode 'r'
ω	forcing frequency
ω_r	natural frequency of mode 'r'

Appendix I

The basis of equation (1) is derived from the summation of force and moment of a basic beam (refer to Figure 1(b)) subjected to dynamic loading, as shown in Figure A.1. The geometric and physical parameters of the rotor are as shown in Figure 10.

The summation of force in vertical axis acting on differential elements and moments at point A due to inertial forces per unit length $f(x, t)$, is given as:

$$V(x, t) - \left[V(x, t) + \frac{\partial V(x, t)}{\partial x} dx \right] - f(x, t) dx = 0 \quad (30)$$

$$M(x, t) + V(x, t) dx - \left[M(x, t) + \frac{\partial M(x, t)}{\partial x} dx \right] = 0 \quad (31)$$

For base motion and $f(x, t) = m \frac{\partial^2 w(x, t)}{\partial t^2}$, equations (30) and (31) are given as:

$$\frac{\partial V(x, t)}{\partial x} = m \frac{\partial^2 w(x, t)}{\partial t^2} \quad (32)$$

$$\frac{\partial M(x, t)}{\partial x} = V(x, t) \quad (33)$$

Solving equations (32) and (33) simultaneously results in equation (1) in the Steady-state response of cantilevered Euler-Bernoulli beam model under harmonic base excitation using modal model approach section. It is noted that the moment is not only due to the strain of the material but also its strain rate, denoted as $\dot{\epsilon}$ and leads to the moment in Figure 10 as:

$$M(x, t) = EI \left(\frac{\partial^2 w(x, t)}{\partial x^2} + \alpha \frac{\partial^2 w(x, t)}{\partial x^2 \partial t} \right) \quad (34)$$

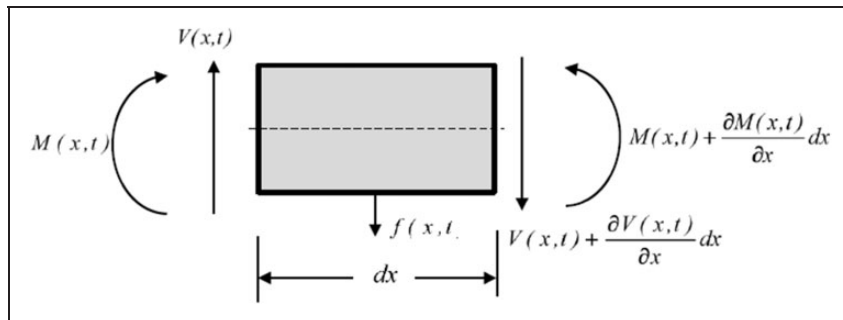


Figure 10

which relates to the following equations (equation (35a–c))

$$\sigma = E(\epsilon + \alpha \dot{\epsilon}), \quad \frac{\epsilon}{c} = \frac{\partial^2 w(x, t)}{\partial x^2} \quad \text{and} \quad M = \frac{\sigma I}{c} \quad (35a, b, c)$$

where c is the half-thickness of the beam, α is damping constant, and σ is stress of the structure. Thus, equation (1) turns into equation (36):

$$EI \frac{\partial^4 u(x, t)}{\partial x^4} + c_s I \frac{\partial^5 u(x, t)}{\partial x^4 \partial t} + c_a \frac{\partial u(x, t)}{\partial t} + m \frac{\partial^2 u(x, t)}{\partial t^2} = 0 \quad (36)$$

The additional damping velocity due to air particle c_a and c_s is αE . Using the relationship between absolute and base motions (equation (2)), the above equation becomes:

$$\begin{aligned} EI \frac{\partial^4 u_{rel}(x, t)}{\partial x^4} + c_s I \frac{\partial^5 u_{rel}(x, t)}{\partial x^4 \partial t} + c_a \frac{\partial u_{rel}(x, t)}{\partial t} \\ + m \frac{\partial^2 u_{rel}(x, t)}{\partial t^2} \\ = -EI \frac{\partial^4 u_b(x, t)}{\partial x^4} - c_s I \frac{\partial^5 u_b(x, t)}{\partial x^4 \partial t} - m \frac{\partial^2 u_b(x, t)}{\partial t^2} \\ - c_a \frac{\partial u_b(x, t)}{\partial t} \end{aligned} \quad (37)$$

It is noted that u_b along x is constant and its differentiation with respect to x is zero, thus, the first and second terms of RHS of equation (37) vanish, and equation (36) becomes equation (4), as written in Section 2.

Appendix 2

The detailed derivation of equations (4) to (13) is shown here by choosing the first left term of equation (4) as an example. By multiplying the first left term of equation (4) with $\varphi_s(x)$ and integrating it with

respect to x from along 0 to L , $\int_{x=0}^L d(x)$, it is written as:

$$\begin{aligned} & \int_{x=0}^L \varphi_s(x) EI \frac{\partial^4 u_{rel}(x, t)}{\partial x^4} d(x) \\ &= EI \int_{x=0}^L \varphi_s(x) \frac{\partial^4 (\sum_{r=1}^{\infty} \varphi_r(x) \eta_r(t))}{\partial x^4} d(x) \end{aligned} \quad (38)$$

Since $\eta_r(t)$ is given as a function of modal coordinate with respect to time, it can be excluded from the integration and the mass normalised eigenfunction are left to be integrated, where:

$$\begin{aligned} & \int_{x=0}^L \varphi_s(x) EI \frac{\partial^4 u_{rel}(x, t)}{\partial x^4} d(x) \\ &= EI \eta_r(t) \int_{x=0}^L \varphi_s(x) \frac{\partial^4 (\sum_{r=1}^{\infty} \varphi_r(x))}{\partial x^4} d(x) \end{aligned} \quad (39)$$

It is known that $\varphi_r(x)$ is given by equation (8), $\frac{\partial^4 (\sum_{r=1}^{\infty} \varphi_r(x))}{\partial x^4}$ is then given as:

$$\frac{\partial^4 \left(\sqrt{\frac{1}{mL}} \left[\cosh \frac{\lambda_r}{L} x - \cos \frac{\lambda_r}{L} x - \sigma_r \left(\sinh \frac{\lambda_r}{L} x - \sin \frac{\lambda_r}{L} x \right) \right] \right)}{\partial x^4} \quad (40)$$

which gives,

$$\frac{\partial^4 (\sum_{r=1}^{\infty} \varphi_r(x))}{\partial x^4} = \frac{\lambda_r^4}{L^4} \varphi_r(x) \quad (41)$$

Equation (38) then turns into equation (42), as follows:

$$\begin{aligned} & \int_{x=0}^L \varphi_s(x) EI \frac{\partial^4 u_{rel}(x, t)}{\partial x^4} d(x) \\ &= EI \frac{\lambda_r^4}{L^4} \eta_r(t) \int_{x=0}^L \varphi_s(x) \varphi_r(x) d(x) \end{aligned} \quad (42)$$

The integration term in equation (42) can be simplified by equating it to equation (10) and multiplying

both the denominator and numerator by m ,

$$\begin{aligned} & \int_{x=0}^L \varphi_s(x) EI \frac{\partial^4 u_{rel}(x, t)}{\partial x^4} d(x) \\ &= EI \frac{\lambda_r^4}{mL^4} \eta_r(t) \int_{x=0}^L m \varphi_s(x) \varphi_r(x) d(x) \end{aligned} \quad (43)$$

It can be seen that the integration term in the left-hand side of equation (43) is similar to equation (10), while the term $EI \frac{\lambda_r^4}{mL^4}$ can be simplified by relating it to equation (12), thus equation (43) becomes:

$$\int_{x=0}^L \varphi_s(x) EI \frac{\partial^4 u_{rel}(x, t)}{\partial x^4} d(x) = \eta_r(t) \quad (44)$$

where,

$$\omega_r^2 = \lambda_r^4 \frac{EI}{mL^4} \quad \text{and} \quad \int_{x=0}^L m \varphi_s(x) \varphi_r(x) d(x) = \delta_{rs} = 1 \quad (45a,b)$$

Same derivation process from equations (38–45) is also applied to the second until fourth terms of equation (4), simplified as follows:

Second term:

$$\int_{x=0}^L \varphi_s(x) c_s I \frac{\partial^5 u_{rel}(x, t)}{\partial x^4 \partial t} d(x) = \frac{c_s \omega_r^2}{E} \frac{\partial \eta_r(t)}{\partial t} \quad (46)$$

Third term:

$$\int_{x=0}^L \varphi_s(x) c_s I \frac{\partial^5 u_{rel}(x, t)}{\partial x^4 \partial t} d(x) = \frac{c_s \omega_r^2}{E} \frac{\partial \eta_r(t)}{\partial t} \quad (47)$$

Third term:

$$\int_{x=0}^L \varphi_s(x) m \frac{\partial^2 u_{rel}(x, t)}{\partial t^2} d(x) = \frac{\partial \eta_r(t)}{\partial t} \quad (48)$$